

Unconventional localization of light with Mie-tronics

Thanh Xuan Hoang,^{1,*} Daniel Leykam,² Ayan Nussupbekov,¹ Jie Ji,³ Jaime Gómez Rivas,³ and Yuri Kivshar⁴

¹*Institute of High Performance Computing, A*STAR (Agency for Science, Technology and Research), Singapore*

²*Science, Mathematics and Technology Cluster, Singapore University of Technology and Design, Singapore*

³*Department of Applied Physics and Science Education, Eindhoven University of Technology, The Netherlands*

⁴*Nonlinear Physics Center, Research School of Physics, Australian National University, Australia*

(Dated: July 17, 2025)

Localization of light requires high- Q cavities or spatial disorder, yet the wave nature of light may open novel opportunities. Here we suggest to employ *Mie-tronics* as a powerful approach to achieve the hybridization of different resonances for the enhanced confinement of light via interference effects. Contrary to a conventional approach, we employ the symmetry breaking in finite arrays of resonators to boost the Q factors by in-plane multiple scattering. Being applied to photonic moiré structures, our approach yields a giant enhancement of the Purcell factor via twist-induced coupling between degenerate collective modes. Our findings reveal how finely tuned cooperative scattering can surpass conventional limits, advancing the control of wave localization in many subwavelength systems.

Introduction.—Wave propagation and wave localization have long fascinated scientists, shaping our understanding of natural phenomena and enabling technologies across classical optics, acoustics, and quantum systems. Even the simplest case—such as scattering of waves by point scatterers and spheres—have inspired theoretical advances from the pre-Maxwell era to the modern rise of Mie-tronics [1, 2]. It is now widely recognized that wave localization arises from coherent multiple scattering and interference of several waves [3].

Conventional mechanisms for localization of waves fall into one of two broad categories: cavity-based and disorder-induced localization. Cavity-based modes—including whispering-gallery, Fabry-Pérot, and bandgap modes—originate in diverse physical domains, but they have converged conceptually under the shared language of wave physics. Despite their differences, they all rely on reflection-based confinement: internal reflection along curved boundaries, reflection between parallel surfaces, or Bragg reflection in periodic lattices [4].

Disorder-induced (or Anderson) localization, by contrast, is rooted in multiple electron scattering [5], with its optical analogue proposed through a connection between atomic orbitals and Mie resonances [6, 7]. Though several experiments have claimed to observe optical analogues of Anderson localization [8, 9], recent advances in computational electromagnetism and Mie-tronics suggest that the radiative and long-range interaction nature of light may fundamentally prohibit true Anderson localization [10, 11]. In fact, spatial disorder often degrades rather than enhances optical confinement [12], challenging long-standing beliefs and motivating the development of new strategies for efficient localization of light.

Underpinned by the recent progress in nanophotonics and electromagnetic modeling, Mie-tronics emerged as a rigorous scattering-based framework grounded in multipolar expansions—offering a powerful tool for under-

standing and optimizing light localization. Beyond providing a first-principle interpretation of conventional cavity modes [12], it unifies diverse localization mechanisms through multipolar interactions.

Here, we propose unconventional strategies for enhancing localization of light by combining key features of Fabry-Pérot, whispering-gallery, and band-edge resonances. Within the Mie-tronics framework, we show that symmetry breaking in finite arrays—traditionally thought to degrade the Q factor—can instead enhance in-plane multiple scattering, thereby increasing both Q and the Purcell factor. We apply this approach to photonic moiré structures, demonstrating that symmetry breaking lifts degeneracy and enables strong coupling between collective modes, resulting in tight confinement and giant Purcell enhancement. These findings provide an efficient strategy for optimizing localization via hybrid resonances, clarify the origin of flat bands and magic angles in moiré systems [13–15], and offer a compelling alternative to disorder-based localization. Altogether, they establish new design principles for resonant metadevices with broad implications across wave-based technologies beyond photonics.

Resonant Mie-tronics: beyond the Anderson localization.—Lorenz first derived the exact solution for plane wave scattering by a sphere. Later, Mie developed a systematic multipole expansion that established the analytical foundation for the modern scattering theory [16, 17]. Over the past four decades, research on light localization via Mie scattering has followed two main directions: (i) disorder-driven Anderson mechanisms [10], and (ii) coupling between Mie scatterers [18]. Early in the development of photonic crystals, it was argued that such coupling would hinder localization [19]. Contrary to this view, we show that optical coupling is essential for efficient light localization. More fundamentally, we demonstrate that the long-range nature of electromagnetic interactions—and the positive energy of electromagnetic waves—precludes true Anderson localization of light. To show this, we begin with key analytical results from multipole expansions,

* hoangxuan11@gmail.com

underpinning Mie-tronics [20].

The electromagnetic field inside a dielectric resonator can be expanded either in terms of regular electric \mathbf{N}_{lm} and magnetic \mathbf{M}_{lm} multipole fields, or equivalently in terms of plane waves, as follows [21, 22]:

$$\mathbf{E}(\mathbf{r}) = \sum_{l=1}^L \sum_{m=-l}^l [\zeta_{lm} \mathbf{N}_{lm}(k\mathbf{r}) + \eta_{lm} \mathbf{M}_{lm}(k\mathbf{r})] \quad (1)$$

$$= \frac{ik}{2\pi} \int_0^{2\pi} d\beta \int_0^\pi d\alpha \sin \alpha \hat{E}(\hat{s}) e^{i\mathbf{k} \cdot \mathbf{r}}, \quad (2)$$

where ζ_{lm} and η_{lm} are the multipole expansion coefficients, related to the spectral amplitude $\hat{E}(\hat{s})$ through its expansion in vector spherical harmonics. The wave vector of each plane wave is $\mathbf{k} = k\hat{s} = k(s_x, s_y, s_z) = k(\sin \alpha \cos \beta, \sin \alpha \sin \beta, \cos \alpha)$, where k is the wave number. The truncation order L is determined by the size of the resonator. These representations, Eqs. (1) and (2), are applicable to resonators of arbitrary shape and size. Since dielectric resonators must radiate [23], the internal field in Eq. (1) acts as a secondary source that emits electromagnetic waves into the surrounding medium.

When a resonator comprises multiple Mie scatterers, coupling between their multipole moments is governed by the translational addition theorem [24, 25]. For instance, for two on-axis scatterers, an electric dipole (ED) $\mathbf{N}_{1,1}$ from one scatterer can induce a magnetic dipole (MD) $\mathbf{M}_{1,1}$ in the other through a translational coupling coefficient:

$$B_{1,1}^{1,1} = \frac{\sqrt{3}}{2} e^{ikd} \left(\frac{i}{kd} - \frac{1}{(kd)^2} \right), \quad (3)$$

where d is the center-to-center distance between the two scatterers. Equations (2) and (3) are central to understanding the nature of light localization in Mie scattering systems such as those shown in Fig. 1.

The wave number in Eq. (2) is purely real and positive, indicating that the light wave is a propagating mode and does not decay exponentially in all three dimensions (3D), unlike Anderson localization of electrons. Moreover, Anderson localization theory assumes that the interaction strength between scatterers decays faster than $1/d^3$, which justifies neglecting long-range interactions and focusing on short-range coupling [5]. In contrast, the interaction in Eq. (3) decays with a leading order of $1/d$, violating this assumption. The slow decay renders long-range interactions an intrinsic feature of light localization, fundamentally altering the confinement mechanism [20]. It also explains the failure of tight-binding models to accurately describe photonic mode coupling [11, 26], even in systems composed of high- Q coupled resonators [25, 27].

More recently, much interest in light localization has centered on the concept of symmetry-protected bound states in the continuum (BICs), which—unlike Anderson localization—rely on optical coupling between unit cells [28]. In such systems, perfect in-plane confinement is

attributed to symmetry-prohibited radiation, and breaking that symmetry is widely believed to destroy localization. However, Mie-tronics reveals a contrasting picture: symmetry breaking can, in fact, enhance localization.

Beyond Bloch: enhanced localization via asymmetry.—Figure 1(a) shows a typical photonic crystal slab interacting with an out-of-plane MD emitter, producing a vortex beam [29]—labeled BIC. This exemplifies light confinement within the Bloch wave framework. From a Mie-tronics perspective, the unit cell in the right inset of Fig. 1(a) is functionally equivalent to the three unit cells shown in Fig. 1(b). These geometries, adapted from previous studies [11, 30, 31], support the same collective MD resonances despite differing shapes [20]. Building on this equivalence, we find that breaking symmetry—contrary to conventional expectations [32]—can enhance both the Purcell and Q factors by strengthening in-plane multiple scattering via engineered multipole couplings, a hallmark of Mie-tronics.

We begin by analyzing Bloch modes excited by a MD source (m_x) placed at the center of each unit cell, with Bloch boundary conditions applied along the y and z directions. Owing to the orthogonality of multipole modes, the source initially excites only the intrinsic MD resonance, as the internal field at the unit cell center is given by $\eta_x = \sqrt{\frac{3}{8\pi}} \lambda H_x$ [33]. This primary excitation subsequently induces higher-order multipoles through optical coupling, capturing the multiple-scattering processes mediated by the Bloch boundaries. This is fully accounted for in our analysis [20].

Figure 1(c) shows that near the Γ point, the Q factors of the Bloch modes diverge for the sphere, square, and hole photonic crystals, indicating the presence of at- Γ BICs. By contrast, the T-shaped photonic crystal exhibits a finite Q factor at the Γ point. This aligns with conventional wisdom: symmetry breaking degrades light confinement by opening radiative leakage channels, thereby reducing the Q factor [34].

Surprisingly, in finite arrays of Mie scatterers, symmetry breaking enhances confinement by strengthening in-plane multiple scattering. As shown in Fig. 1(d), the T-shaped array exhibits the highest Q factor among all geometries for array sizes up to 33×33 unit cells—reversing the trend predicted by the Bloch mode analysis.

This Q enhancement arises from stronger in-plane optical coupling, as revealed by the far-field radiation patterns in Figs. 1(e,f). The square array radiates primarily out of plane, forming a dominant out-of-plane channel. By contrast, the T-shaped unit cell redistributes radiation into in-plane channels, boosting the Q factor by over an order of magnitude compared to the hole and sphere arrays. Yet this same symmetry breaking also increases radiation into other directions, ultimately causing the Q factor to saturate for larger arrays, as seen in Fig. 1(d). These findings highlight the importance of engineering cooperative scattering in finite metastructures to optimize light confinement beyond the Bloch wave paradigm.

High- Q Localization via Hybrid Super-Resonances.—

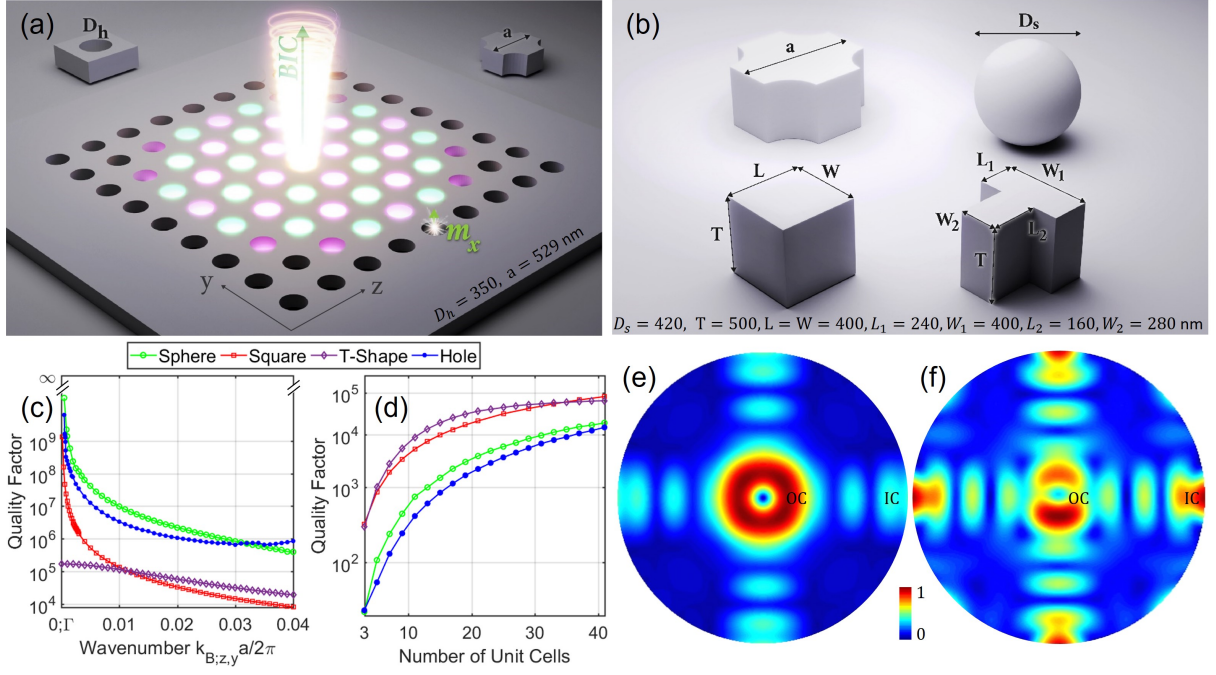


FIG. 1. Symmetry breaking enhances light confinement in finite-extend photonic crystals. (a) Schematic of an out-of-plane magnetic dipole (m_x) interacting with an array of air holes in a silicon slab (refractive index 3.5). Insets show unit cells and their geometrical parameters. (b) Four functionally equivalent unit cells used in this study. The T-shaped unit cell is derived from the square unit cell by breaking in-plane symmetry. (c) Q factors of Bloch modes at the Γ point, showing that symmetry breaking reduces the infinite Q of the square unit cell to a finite value in the T-shaped unit. (d) Q factors of collective resonances in finite-sized arrays. Square and T-shaped arrays support substantially higher Q values than hole and sphere arrays. Symmetry breaking enhances light confinement in the T-shaped array for array sizes ranging from 5 to 33. (e) Far-field radiation pattern from a 9×9 square array excited by m_x , showing a vortex beam profile. (f) Same as (e) but for the T-shaped array, revealing enhanced in-plane multiple scattering along in-plane channels (ICs) compared to out-of-plane channels (OCs).

Beyond offering practical insights into high- Q resonances, Mie-tronics provides a systematic framework for their optimization. We illustrate this by examining light localization in hole arrays, such as the example shown in Fig. 2(a) [30]. Among the geometries studied, finite hole arrays are the least effective at confining light [Fig. 1(d)], as the slab acts as an effective waveguide, allowing in-plane leakage to escape efficiently. However, we show that this leakage can be harnessed: by redirecting it back toward the array center, one can achieve strong confinement through hybrid super-resonances.

Figure 2(b) shows the Purcell factor spectra for three configurations: (1) a central 17×17 hole array functioning as a cavity, surrounded by four mirror arrays that redirect in-plane leakage back into the cavity; (2) a stand-alone 17×17 hole array without mirrors; and (3) a larger 37×37 hole array without mirrors. Configuration (1) exhibits an order-of-magnitude enhancement in the Purcell factor compared to (2) and (3), demonstrating the effectiveness of hybrid confinement. Conventionally, this enhancement is attributed to a photonic bandgap induced by the different periodicity of the mirror arrays, which backreflect in-plane leakage and promote localization within the central array [30].

While this photonic crystal-based design boosts the

Purcell factor from below 50 to over 500, Mie-tronics offers a more direct and flexible strategy for Q optimization, as illustrated in Fig. 2(e). In Mie-tronics, the number of unit cells governs the detuning between the collective responses of the mirrors and the cavity, thereby controlling the backscattering strength. As a result, even when cavity and mirror arrays share the same period ($a_C = a_M$), fine-tuning a single geometric parameter—the mirror-cavity gap G_{MC} —can yield a similar Q enhancement. In both cases, adjusting G_{MC} leads to a two-order-of-magnitude increase in the Q factor.

The effects of mirror fine-tuning on the near- and far-field profiles are shown in Figs. 2(c) and 2(d). Mirrors enhance the near-field intensity by more than an order of magnitude through coherent backscattering of in-plane leakage, as evidenced by the far-field patterns in the insets. Compared to Fig. 2(c), the far-field distribution in Fig. 2(d) exhibits stronger scattering into large-angle directions near the periphery.

The mirrors reshape the topology of the vortex pattern—a hallmark of strong coupling. In Mie-tronics, strong coupling emerges through the coalescence of resonances [11]. To confirm this mechanism for enhanced light localization, we plot the Purcell factor for three gap sizes in Fig. 2(f). For suboptimal gaps of $G_{MC} = 521$ nm

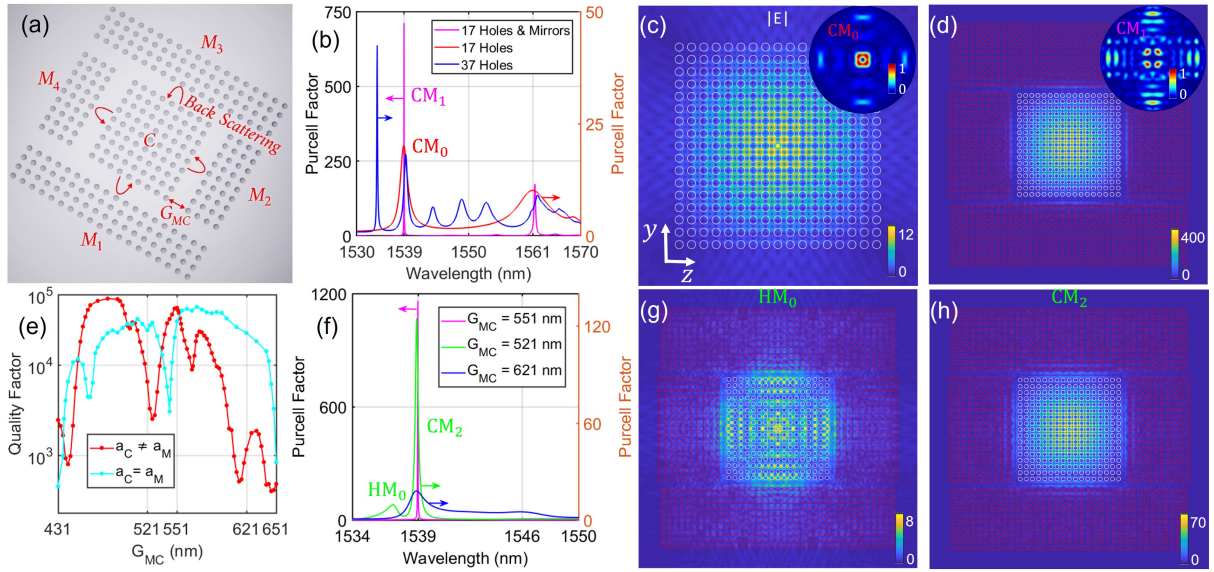


FIG. 2. Purcell factor enhancement by merging hybrid and collective modes. (a) Supercavity metastructure consisting of a central hole array (C) acting as the cavity resonator, surrounded by four mirror arrays ($M_{1,2,3,4}$) that scatter light back into the cavity region. (b) Purcell factor spectrum for a magnetic dipole (m_x) placed at the center of the cavity. Fine-tuning the mirror gap to $G_{MC} = 541$ nm boosts the Purcell factor by over an order of magnitude at the CM_0 and CM_1 resonances. (c) and (d) Electric field distributions of the CM_0 and CM_1 modes, showing strong field confinement and over tenfold enhancement at the center due to mirror tuning. Insets: corresponding far-field patterns. (e) Dependence of Q -factor enhancement on the gap size G_{MC} for two cases: (1) mirror arrays with a slightly larger period ($a_M = 552$ nm) than the cavity ($a_C = 529$ nm), and (2) identical periods ($a_M = a_C = 529$ nm). Both exhibit similar Q enhancement. (f) Purcell factor spectra for three gap values, revealing that the Q boost arises from the coalescence of two resonances: HM_0 and CM_2 . (g) and (h) Electric field distributions of HM_0 and CM_2 , highlighting their distinct spatial profiles.

and $G_{MC} = 621$ nm, there are two distinct resonances, HM_0 and CM_2 . The frequency of CM_2 is nearly independent of the gap size, being dictated by the central array, while HM_0 redshifts with increasing G_{MC} , characteristic of a Fabry-Pérot mode. The Purcell factor reaches its maximum when these two modes coalesce at $G_{MC} = 551$ nm, coinciding with the Q -factor peak in Fig. 2(e).

Field profiles in Figs. 2(g,h) further clarify the nature of these resonances. HM_0 exhibits Fabry-Pérot-like backreflection, but its near-field structure is intrinsically shaped by Mie scattering, making it a hybrid mode. CM_2 also displays hybrid character, though its field pattern closely resembles the collective mode shown in Fig. 2(c). At resonance coalescence, HM_0 functions as an auxiliary channel that constructively reinforces CM_2 , leading to enhanced confinement.

We show in the Supplementary Material [20] that hybridizing Fabry-Pérot and Mie resonances (whispering-gallery modes) produces additional hybrid modes that inherit advantageous features from both mechanisms, enabling unconventional forms of light localization. Interestingly, we find that simple reflective terminations at the edges can also enhance the Q factor of collective modes (Fig. S6), though to a lesser extent than the hole-array mirrors in Fig. 2, due to the lack of collective backscattering. However, these edge reflectors offer a distinct advantage: they allow substantial miniaturization of the

resonator footprint. Since miniaturization is essential for integrated photonics, this capability marks a central theme of subwavelength Mie-tronics. This raises a natural question: given a fixed number of scatterers—such as a 17×17 hole array, can we strategically reconfigure them into a smaller footprint while further enhancing both the Purcell and Q factors?

A promising answer emerges by drawing inspiration from a seemingly unrelated domain—twisted bilayer graphene—where spatial reconfiguration and interference similarly lead to extreme localization.

Localization through strong coupling.—In twisted bilayer graphene, electrons become strongly localized at specific twist angles—so-called magic angles—leading to van Hove singularities in the local density of states [35, 36]. History appears to repeat itself, as electronic magic angles have quickly inspired analogous explorations in photonics [37, 38]. Yet, despite over a decade of intense investigation, the physical origin of magic angles remains unresolved [13, 15]. A major obstacle is the computational intractability of full-scale electronic structure calculations [36], which has led to the widespread use of simplified tight-binding models. However, these models—built upon differing assumptions—often yield inconsistent predictions for both the value and nature of the magic angles [15].

Here, we turn to Mie-tronics and employ full-wave elec-

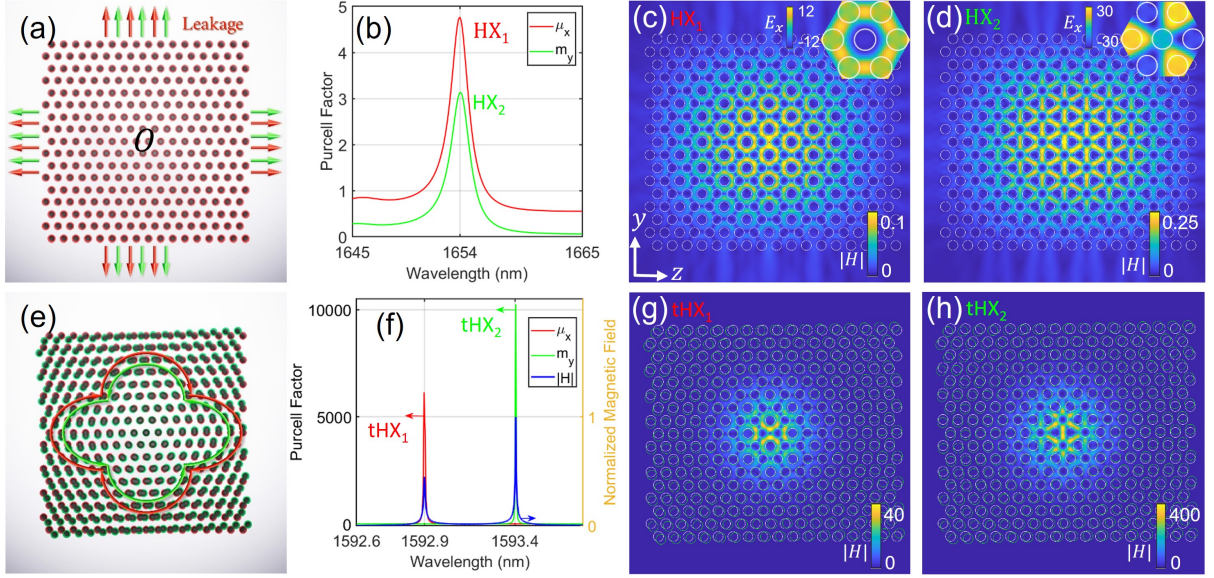


FIG. 3. Twisted Mie-tronics. (a) Schematic of a hexagonal hole array, inspired by the graphene lattice; red circles indicate air holes. (b) Purcell spectra for electric (μ_x) and magnetic (m_y) dipoles placed at point O in (a), showing two degenerate collective modes, HX_1 and HX_2 . (c) and (d) Magnetic field profiles of HX_1 and HX_2 reveal distinct spatial patterns; insets show their respective E_x field symmetries (symmetric and antisymmetric). (e) Twisted hexagonal structure formed by overlaying a second, rotated copy (green circles) of the original array. (f) Twisting couples the degenerate modes into hybridized states, resulting in twisted HX_1 (tHX_1) and HX_2 (tHX_2). (g) and (h) Magnetic field distributions of the twisted modes, tHX_1 and tHX_2 , confirming their origin. Twisting enables strong coupling between degenerate band-edge modes—analogue to electronic localization in twisted bilayer graphene.

tromagnetic simulations to investigate photonic magic angles directly. Owing to the shared wave nature of electrons and photons, our findings may shed light on the elusive origin of electronic magic angles.

A seemingly straightforward strategy is to twist the square hole array shown in Fig. 2(c). This twist leaves the central holes relatively unchanged while significantly altering the outer holes. By modifying the outer holes, one might expect their collective response to differ from that of the central holes, potentially reflecting part of the in-plane leakage and enhancing confinement, similar to the effect observed in Fig. 2. However, this strategy fails because twisting disrupts the phase coherence among the multipolar waves emitted by different scattering centers, thereby weakening the collective resonances [12].

The failure of the square lattice to sustain strong collective resonances under twisting highlights the importance of lattice geometry in enabling wave localization—particularly the hexagonal arrangement found in twisted bilayer graphene. Upon rearranging the square hole array into a hexagonal configuration, we observe pronounced mode localization driven by twisting, shown in Figs. 3 and 4. This enhanced localization arises because the hexagonal geometry supports two degenerate collective resonances, marked as HX_1 and HX_2 in Fig. 3(b), akin to the degeneracies that facilitate magic-angle effects in twisted two-dimensional electronic crystals [15].

Figures 3(c,d) show the near-field distributions of the

transverse magnetic modes HX_1 and HX_2 , which require excitation by an ED emitter (μ_x) or a MD emitter (m_y), respectively. This source-dependent excitation arises because, in periodic arrays, modes of different symmetry classes typically decouple [39]. The insets of Figs. 3(c,d) show that the electric fields of HX_1 and HX_2 are symmetric and antisymmetric, respectively, with respect to the centre point, explaining their decoupling. Consequently, a single emitter only excites HX_1 or HX_2 , despite the spectral and spatial overlap of these modes.

In twisted bilayer graphene, two monolayers are stacked to form a moiré superlattice. Although the merged moiré pattern formed by twisted silicon holes in Fig. 3(e) differs geometrically, it functions similarly in terms of wave localization: both induce interband coupling between symmetry-broken modes. In graphene, this coupling is the primary mechanism driving electron localization [15]. Similarly, Fig. 3(f) shows strong coupling between HX_1 and HX_2 at a twist of $\theta = 1.45^\circ$, evidenced by the splitting of the magnetic response spectrum under m_x excitation. The resulting twisted modes, tHX_1 and tHX_2 , exhibit strongly localized magnetic fields (see Figs. 3(g,h)), enhanced by two to three orders of magnitude relative to their untwisted counterparts. This dramatic field enhancement is a hallmark of strong interband coupling, leading to suppressed in-plane leakage via destructive interference and enabling unconventional light localization. Experimental evidence

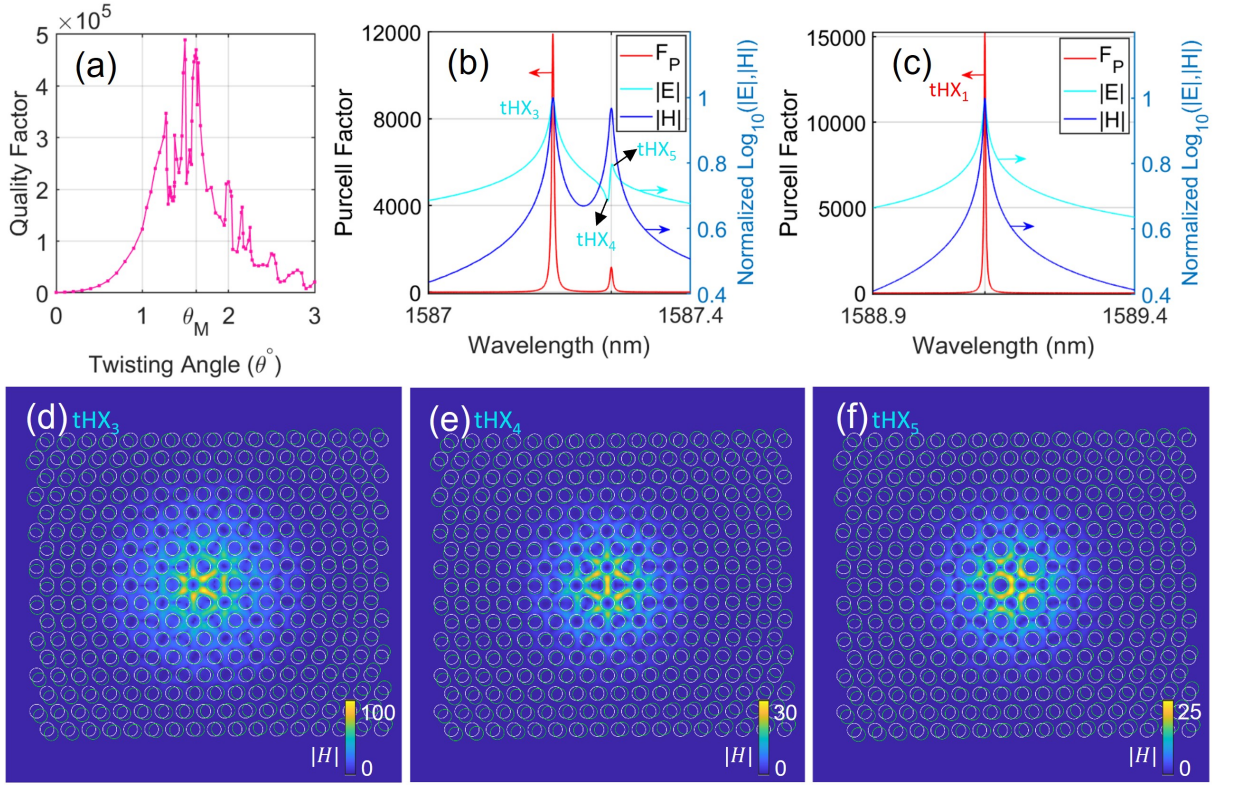


FIG. 4. Magic angles in Mie-tronics. (a) Q factor of the twisted mode originating from the band-edge mode HX_1 as a function of twist angle θ . Multiple peak angles—photonic analogues of the electronic magic angles in twisted bilayer graphene—emerge due to the crossing and splitting of the twisted modes HX_1 and HX_2 . (b) Purcell factor spectrum at a sub-optimal twist angle $\theta = 1.675^\circ$, showing two peaks. The magnetic field trough adjacent to the weaker Purcell peak results from destructive interference between resonances. (c) Spectral profile at the magic angle $\theta_M = 1.6^\circ$, where the dipole μ_x selectively excites only the twisted mode tHX_1 . (d)–(f) Magnetic field distributions at the three wavelengths labeled tHX_3 , tHX_4 , and tHX_5 in (b). Modes tHX_3 and tHX_5 correspond to the two Purcell peaks, while tHX_4 corresponds to the interference-induced trough.

of interband coupling includes the observation of two Van Hove singularities in twisted bilayer graphene [35] and dual lasing modes in photonic moiré lasers [38].

Photonic magic angles.— To identify magic angles, we plot the Q factor of the twisted HX_1 mode as a function of the twist angle θ in Fig. 4(a). Interestingly, beyond 1° , multiple angles correspond to peaks in the Q factor. The maximum Q reaches about five times higher than that shown in Fig. 2, even though the twisted structure occupies only about 18% of the area of the 37×37 hole array. However, for twist angles beyond $\theta > 3^\circ$, the Q factor begins to decrease below 10^4 as the inner unit cells progressively shift out of resonance, counteracting the enhancement provided by interband coupling.

The pronounced fluctuations around the peak angles reflect constructive and destructive interference within the moiré structure. To uncover the origin of these features, we analyze the Purcell and field spectra at two twist angles: a suboptimal value of $\theta = 1.675^\circ$ [Fig. 4(b)] and a peak (magic) angle of $\theta_M = 1.6^\circ$ [Fig. 4(c)]. At $\theta = 1.675^\circ$, two twisted modes— tHX_3 and tHX_5 —appear in both the Purcell and magnetic field spectra, accompanied by a pronounced electric field trough (tHX_4) adja-

cent to the weaker Purcell peak. The field profile of tHX_5 [Fig. 4(f)] reveals its origin in band HX_1 and exhibits destructive interference with tHX_4 , which originates from HX_2 . This suboptimal interference lowers both the Q factor and Purcell enhancement, while also distorting the spatial mode profile of tHX_5 compared to its counterpart in Fig. 3(g). The appearance of tHX_3 [Fig. 4(d)]—also stemming from HX_2 —coincides with the suppression of tHX_4 [Fig. 4(e)], further highlighting strong interband coupling between HX_1 and HX_2 .

At the magic angle $\theta_M = 1.6^\circ$, both tHX_3 and tHX_4 vanish from the spectral plots [Fig. 4(c)], leaving only the dominant mode tHX_1 coupled to the ED emitter μ_x . This dominance, however, does not imply the complete absence of twisted HX_2 modes, which remain accessible via MD excitation (m_y). The behavior underscores the unique character of interband coupling—qualitatively distinct from intraband interactions [11] and from the hybrid supercavity modes in Fig. 2. Photonic magic angles thus arise from the alternating pattern of spectral crossings rather than mode coalescence as the twist angle θ is finely tuned.

Despite the strong localization evident in Figs. 3 and 4,

long-range interactions persist: light continues to extend across multiple unit cells within a single moiré supercell. At the same time, intense field confinement at the supercell centre explains the formation of photonic moiré flatbands [40]. As light is strongly suppressed at the outer holes, neighbouring supercells become effectively decoupled—the overlap integral between their wavefunctions vanishes. Consequently, the resonance frequency becomes independent of the Bloch wavevector, resulting in flat bands [20].

However, the decoupling of neighbouring supercells and the emergence of flatbands do not imply perfect confinement or infinite Q factors. The positive energy of light allows it to radiate, fundamentally limiting the achievable Purcell and Q enhancements in moiré supercavities. Unlike periodic arrays [11, 12], increasing the number of supercells does not lead to divergence, even when bands appear perfectly flat in simulations. This radiative nature and the long-range character of light also explain why disorder generally weakens, rather than enhances, localization [20]. Both John and Anderson acknowledged these features in their foundational theories of disorder-induced localization [3, 19], which have guided decades of attempts to realize Anderson localization of light. Yet, simulating Mie scattering in large, disordered systems remains computationally challenging [7], much like electronic structure calculations in moiré materials [36]. This computational bottleneck has obscured the fundamental role of light’s radiative, long-range nature in shaping its localization behaviour.

With modern computational tools and the analytical framework of Mie-tronics, we conclude that the strongest localization in Mie systems arises from strong coupling between intra- and inter-band resonances, leading to unconventional modes with minimal spatial footprints. Yet even these hybrid modes—combining electric hotspots and flatband resonances—remain sub-exponentially localized [11]. This finding aligns with recent brute-force simulations demonstrating that true exponential Anderson localization is absent in all-dielectric Mie scattering systems [10]. Mie-tronics offers a systematic understanding of how long-range interactions and the radiative nature of light fundamentally constrain localization. Only by accounting for these intrinsic characteristics of light can optimal localization be achieved.

Conclusion.—We have developed a general framework of Mie-tronics as a powerful tool for understanding and optimizing localization of light in subwavelength systems. By combining the advantageous features of multiple resonances (such as Fabry-Pérot, whispering-gallery, and collective Mie modes), we have shown how hybrid super-resonances can substantially enhance both the Q factor and Purcell effect. We clarified the origin of photonic magic angles, showing that twist-induced coupling between degenerate collective modes in moiré structures enhances confinement of light, in analogy to flatbands in a twisted bilayer graphene.

Importantly, while symmetry breaking is tradition-

ally thought to reduce Q factors of resonant lattices, we find that in finite arrays, it can instead enhance Q and strengthen localization via increased in-plane multiple scattering. This challenges conventional photonic crystal theory and opens new routes to high- Q metastructures by tuning cooperative effects. Together, these findings establish Mie-tronics as a strategic foundation for designing next-generation photonic architectures—with implications extending beyond optics to other waves.

ACKNOWLEDGMENTS

This research is supported by the National Research Foundation, Singapore, and A*STAR under its Frontier Competitive Research Programme (NRF-F-CRP-2024-0009), the Australian Research Council (Grant No. DP210101292), and International Technology Center Indo-Pacific (ITC IPAC) via Army Research Office (Contract FA520923C0023). D.L. acknowledges a support from the Ministry of Education of Singapore under its SUTD Kickstarter Initiative (Grant No. SKI 20210501). J. Ji acknowledges the funding received from the PhotonDelta National Growth Fund programme.

Supplemental Material for “Unconventional Localization of Light with Mie-tronics”

I. FUNDAMENTALS OF MIE-TRONICS

A. Analytical and Numerical Tools

Mie theory provides one of the rare exact analytical solutions to Maxwell’s equations, offering Mie-tronics a uniquely rigorous foundation. At its core, Mie-tronics is built on multipole expansions and Mie coefficients, which decompose electromagnetic fields into analytically defined vector spherical harmonics. In the standard formalism, the incident \mathbf{E}^{inc} , scattered \mathbf{E}^{sct} , and internal \mathbf{E}^{int} electric fields are expanded as:

$$\begin{aligned}\mathbf{E}^{\text{inc}}(\mathbf{r}) &= \sum_{l=1}^{L_{\text{inc}}} \sum_{m=-l}^l [p_{lm}\mathbf{N}_{lm}(k\mathbf{r}) + q_{lm}\mathbf{M}_{lm}(k\mathbf{r})], \\ \mathbf{E}^{\text{sct}}(\mathbf{r}) &= \sum_{l=1}^{L_R} \sum_{m=-l}^l [a_l p_{lm}\mathbf{N}_{lm}^{(1)}(k\mathbf{r}) + b_l q_{lm}\mathbf{M}_{lm}^{(1)}(k\mathbf{r})], \\ \mathbf{E}^{\text{int}}(\mathbf{r}) &= \sum_{l=1}^{L_R} \sum_{m=-l}^l [c_l p_{lm}\mathbf{N}_{lm}(nk\mathbf{r}) + d_l q_{lm}\mathbf{M}_{lm}(nk\mathbf{r})],\end{aligned}$$

where a_l and b_l (c_l and d_l) are the external (internal) Mie coefficients that determine how each multipole component scatters or penetrates the sphere. Here, n denotes the refractive index of the sphere, and $k = 2\pi/\lambda$ is the wave number in vacuum, with λ the vacuum wavelength.

When the incident field is analytically described—that is, expressible via a finite multipole order L_{inc} —the solution is fully analytical. In practice, however, the infinite series in the well-known Mie solution must be truncated at a finite order L_R , making the solution implementation semi-analytical. A commonly used empirical formula for choosing L_R for a sphere with radius R is [25]:

$$L_R \approx 2\pi R/\lambda + 4.05\sqrt[3]{2\pi R/\lambda} + 2.$$

For example, a sphere of radius 210 nm in vacuum typically requires L_R between 7 and 10 for wavelengths near 1500 nm. While our main interest lies in the collective responses of the ED and MD modes ($l = 1$), setting $L_R = 1$ is generally insufficient and leads to inaccurate estimates of both Q and Purcell factors. Moreover, when $L_{\text{inc}} > L_R$, incident components with $l > L_R$ cannot couple to internal Mie modes and instead propagate through the system without scattering.

Although Mie theory is strictly valid only for homogeneous spheres, Mie-tronics generalizes this formalism by using the Mie basis to analyze light interaction with subwavelength metastructures. For arbitrary geometries—including hole, square, and T-shaped unit cells considered in this study—full-wave simulations are performed using the finite-difference time-domain (FDTD)

method. In this context, Mie-tronics offers a physically meaningful Mie mode basis for understanding the collective resonances of multipolar modes.

In our FDTD simulations, we employ a uniform mesh size of 25 nm for all unit cells. At the working wavelength of approximately 1500 nm, this corresponds to a spatial resolution of roughly $\lambda/60$. For accurate evaluation of the Purcell factor, simulations are terminated only when the residual electromagnetic energy within the computational domain decays below 10^{-7} . Our full-wave results are validated against our previously developed multipole-based computational framework [12].

B. Mie Coefficients as Building Blocks in Mie-tronics

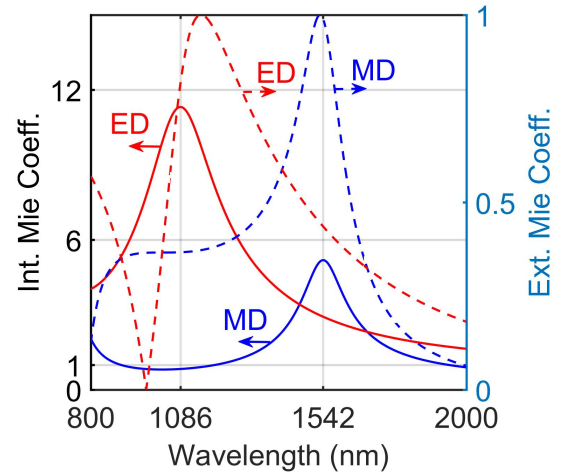


FIG. 5. Spectra of internal (left) and external (right) Mie coefficients for a silicon sphere with a radius of 210 nm and a refractive index of 3.5. The peaks of these coefficients occur at different wavelengths, particularly for the electric dipole mode.

Strictly speaking, a complete analysis of Mie scattering systems requires knowledge of the full multipole expansion coefficients. Nevertheless, the Mie coefficients themselves play a foundational role—not only in the development of the analytical framework but also in governing the overall spectral response of the system. It is therefore essential to examine their spectral characteristics and physical implications.

Figure 5 illustrates the spectral profiles of the two lowest-order Mie coefficients: the magnetic dipole (MD) and the electric dipole (ED). Each mode comprises both external and internal coefficients, arising from the boundary matching of electromagnetic fields across the sphere.

ical interface. Notably, Mie coefficients are derived for stationary (time-harmonic) fields, not for dynamic or transient scenarios. This distinction becomes crucial in applications such as subsurface imaging, where focusing through spherical boundaries is involved [41]. In such cases—particularly for geometries involving open spherical interfaces like hemispheres—the standard Mie formulation is not applicable. Instead, the Debye series must be employed to properly enforce the boundary conditions and yield an accurate physical solution [42].

The history of the Debye series is noteworthy for its role in bridging geometrical optics and wave physics, particularly in explaining multiple scattering within single spheres. Clebsch’s work on the multipole expansion of elastic waves was motivated by the ambition to establish a geometrical optics framework grounded in wave physics—a viewpoint championed by Huygens, Young, and Fresnel. Despite his elegant and rigorous solutions, Clebsch ultimately regarded his efforts as a failure because he was unable to unify geometrical optics with wave physics [1]. A similar challenge emerged in the interpretation of whispering-gallery modes. These were initially explained via geometrical optics until Rayleigh, building on Debye’s formulation, offered a complete wave-based description [43].

The internal ED and MD resonances in Fig. 5 exhibit broad spectral distributions. In the special case of a sphere with an index contrast of one, the internal Mie coefficients are identically one. Hence, coefficients exceeding unity indicate enhanced energy storage. The ED mode resonates across nearly the entire 1200 nm range, while the MD mode spans from 1200 nm to 1940 nm. These broad distributions enable the hybridization of distinct Mie modes, allowing for the exploration of diverse collective resonances.

Despite their broad spectral characteristics, these ED and MD resonances are fundamentally identical to whispering-gallery modes, whether analyzed from a geometrical or wave optics perspective. In early photonic crystal research, it was often believed that coupling large unit cells would not form band structures, since geometrical optics was thought to dominate in that regime [3]. Mie-tronics challenges this notion: all Mie modes inherently embody wave physics and can resonate collectively. As demonstrated in our earlier work, coupling these resonances—whether low-order or high-order—leads to photonic band formation [25, 44].

In Mie-tronics, the Debye series describes multiple internal reflections within a single sphere, where resonant enhancement or suppression of Mie coefficients stems from constructive or destructive interference between partial multipole waves. This reveals that coherent multiple scattering and interference underpin even individual Mie resonances. Next, we show that coupling among Mie resonances leads to spectral splitting near the peak wavelengths of their Mie coefficients, highlighting the necessity of analyzing multipole expansion coefficients—not just the scalar Mie coefficients—when studying collective optical phenomena in Mie systems.

C. Beyond Bloch and Wannier Descriptions

Modern wave theories in photonics often adopt concepts originally developed for electrons, reflecting the historical success of solid-state physics [7]. A key example is the use of Wannier functions, which were introduced to complement Bloch waves by capturing electronic localization in crystals [45]. These have since been extended to photonics [37], despite fundamental differences between light and electrons. While Bloch waves provide an intuitive framework for electron transport, they neglect the atomic-scale structure of matter [46]. Wannier functions address this by constructing spatially localized basis functions from multiple Bloch states, and are now central to electronic structure calculations in finite systems [47].

Photonic systems differ profoundly from electronic ones. Unlike the short-range (nearsighted) couplings assumed in tight-binding models [47], light exhibits long-range electromagnetic interactions. In finite-sized photonic arrays, collective resonances arise from coherent superpositions of plane waves or multipole fields, rather than from localized orbitals or tight-binding overlaps [12]. To illustrate this distinction, we consider a cluster of scatterers excited by a dipolar emitter oriented along the z -axis at the origin O , with dipole moment $\mu_{1;0}$. The scattering field from the n -th sphere, located at position O_n , is described by multipole expansion coefficients $p_{l'm'}^{(n)}$ and $q_{l'm'}^{(n)}$. These coefficients result from two sources: direct excitation by the emitter, and indirect excitation via the scattered fields from all other spheres. The latter are represented by the coefficients $p_{lm}^{(u)}$ and $q_{lm}^{(u)}$ of the u -th scatterer. The induced multipoles follow the following coupling equations [25]:

$$p_{l'm'}^{(n)} = a_{l'}^{(n)} \left(A_{l'm'}^{1;0}(\overrightarrow{OO_n})\mu_{1;0} + \sum_{u \neq n} \sum_{l=1}^{L_u} \sum_{m=-l}^l \left[A_{l'm'}^{lm}(\overrightarrow{O_uO_n})p_{lm}^{(u)} + iB_{l'm'}^{lm}(\overrightarrow{O_uO_n})q_{lm}^{(u)} \right] \right) \quad (4)$$

$$q_{l'm'}^{(n)} = b_{l'}^{(n)} \left(-iB_{l'm'}^{1;0}(\overrightarrow{OO_n})\mu_{1;0} + \sum_{u \neq n} \sum_{l=1}^{L_u} \sum_{m=-l}^l \left[A_{l'm'}^{lm}(\overrightarrow{O_uO_n})q_{lm}^{(u)} - iB_{l'm'}^{lm}(\overrightarrow{O_uO_n})p_{lm}^{(u)} \right] \right). \quad (5)$$

The translational coupling coefficients $A_{l'm'}^{lm}$ and $B_{l'm'}^{lm}$ in Eqs. (4) and (5) encode the long-range electromagnetic interactions, similar to Eq. (3). These terms govern the interference conditions at the n -th scatterer and are essential for capturing the cooperative nature of light scattering. Crucially, the discrete summations in these expressions offer a conceptual clarity and analytical tractability often lacking in integral-based methods such as Wannier functions or plane-wave expansions. This discreteness highlights a key advantage of Mie-tronics in studying localization and interference phenomena in resonant photonic systems.

Within Mie-tronics, both propagating and localized modes emerge from a unified physical basis—multipole and plane-wave expansions, as expressed in Eqs. (1) and (2) in the main text—without relying on artificial constructs such as orbital overlaps. This framework respects the radiative, long-range nature of light and provides an analytically grounded alternative to Bloch-mode integrals and Wannier-type approximations. It exposes the conceptual limitations of importing tight-binding intuition into photonics and underscores the need for first-principles analysis in understanding light localization.

D. Probing Light Localization

Early studies of Anderson localization of light commonly employed plane-wave excitation (e.g., laser beams), using transmission decay as a primary observable. In principle, exponential attenuation of transmission with increasing sample thickness is a signature of Anderson localization [8]. However, this approach has long been questioned due to the inherent presence of material absorption [48, 49]. At the time, the limited availability of computational resources precluded full-wave simulations capable of distinguishing absorption-induced losses from localization effects [7].

With modern computational methods, full-wave simulations using lossless dielectric scatterers (i.e., real-valued refractive indices) can now isolate the role of scattering. Recent results suggest that the radial (longitudinal) components of the electric field hinder true Anderson localization of light [50]. Within the Mie-tronic formalism, the absence of Anderson localization arises more fundamentally from Eqs. (2) and (3) in the main text, which reflect the nature of electromagnetic waves: they carry positive energy, interact via long-range radiative fields, and cannot be exponentially confined in three dimensions.

Advances in metasurface design have further complicated the interpretation of localization experiments. For instance, a single metasurface layer can exhibit zero transmission, even in the absence of localization. This underscores a limitation of transmission-based measurements as conclusive indicators of Anderson localization.

This work adopts a dipole-source excitation approach within the Mie-tronics framework. Unlike plane waves, dipole sources couple to all available photonic modes, en-

abling direct probing of local field confinement in three dimensions. This methodology emulates experimental setups employing quantum emitters [51], and builds on early distinctions between dipole and plane-wave fields that predate Maxwell’s equations [1]. We have previously shown that dipole excitation provides a more faithful assessment of spatial confinement in photonic systems [12].

To investigate disorder-induced effects, we introduce pseudo-random perturbations to the geometric parameters of moiré cavities. Our simulations reveal that disorder consistently weakens localization, in agreement with our analytical predictions. These results challenge prevailing assumptions rooted in electronic analogies and highlight the importance of electromagnetic coherence. Notably, Mie’s original theory was developed for light scattering in turbid media containing metallic inclusions, and our conclusions naturally extend to systems involving random metal scatterers.

It is also instructive to revisit transverse Anderson localization [52], which closely resembles the evanescent field decay described by Lord Rayleigh in infinite dielectric cylinders [53]. In such configurations, field confinement occurs transversely while propagation along the longitudinal axis remains intact—an outcome consistent with the physical implications of Eqs. (1) and (2) in the main text. However, when these waveguides are truncated (e.g., Fabry–Pérot cavities) or curved (e.g., whispering-gallery modes), radiation losses inevitably arise, thereby preventing true three-dimensional exponential localization [23].

These insights support a core principle of Mie-tronics: that electromagnetic waves, by virtue of their long-range radiative nature, do not undergo true Anderson localization. Acknowledging these constraints is essential for advancing light localization strategies grounded in the fundamental physics of wave scattering.

II. COLLECTIVE MIE RESONANCES AND THEIR ROLE IN PHOTONIC CRYSTAL BANDS

In this section, we analyze photonic crystals through the lens of Mie-tronics, highlighting the collective nature of the arrays of the four unit cell types discussed in the main text. Despite differences in shape and size, these arrays all support the same collective MD resonances and photonic crystal bands, though spectrally distinct. This analysis further underscores how multipolar couplings drive the formation of the Bloch bands.

Figure 6(a) presents the Purcell factor associated with the interaction schematic shown in the inset, where the magnetic dipole m_x interacts with a 5×5 sphere array. The spectral profile reveals two distinct bands with three peaks labeled A_1 , A_2 , and B_1 , which correspond to bands located above and below the light line, as shown in the photonic crystal band structure in Fig. 6(d). To further explore these bands, we show the near- and far-field distributions for the A_1 mode in Figs. 6(b) and 6(c), and

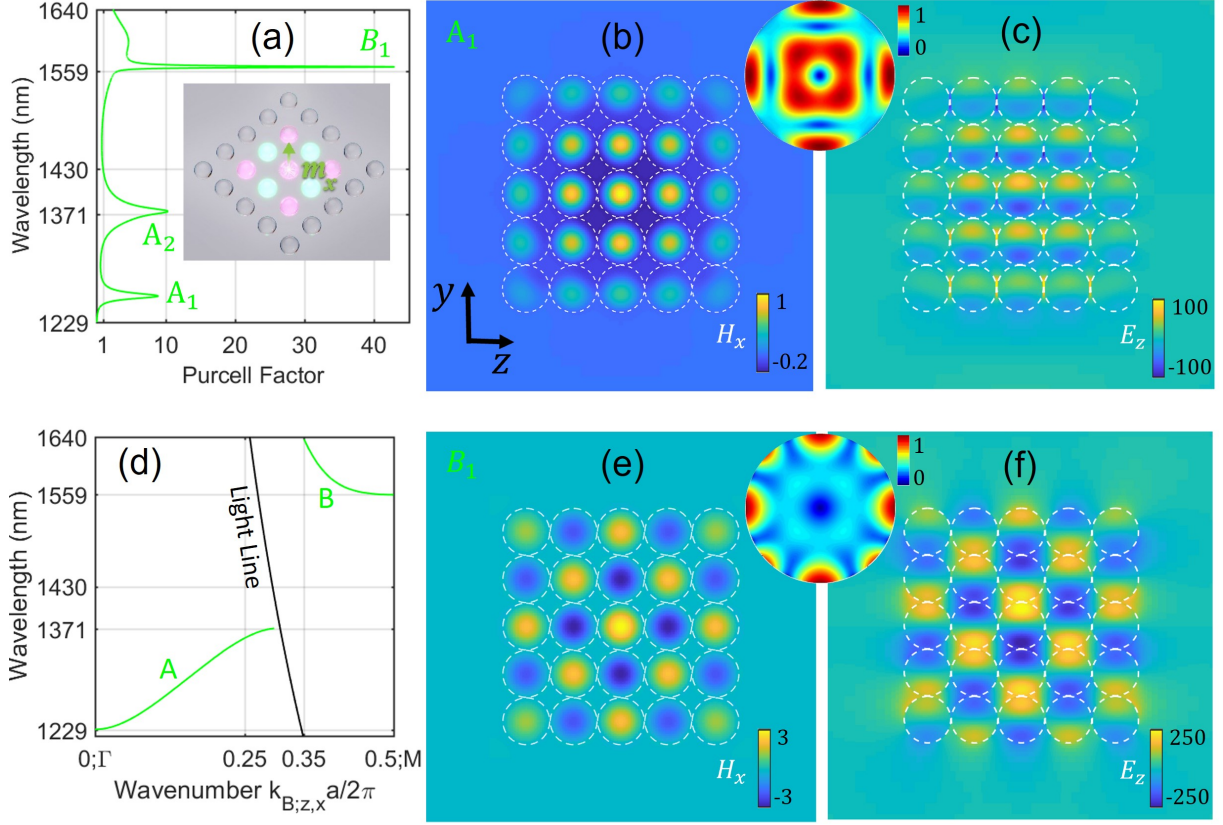


FIG. 6. Collective antibonding and bonding resonances in Mie-tronics and their corresponding Bloch bands. (a) Spectral profile of the Purcell factor associated with the m_x dipole at the center of a 5×5 sphere array, showing two well-separated bands with pronounced peaks labeled $A_{1,2}$ and B_1 . The inset illustrates the interaction schematic. (b) and (c) Magnetic H_x and electric E_z field distributions for the A_1 peak depicted in (a). The E_z distribution highlights the antibonding nature of the A_1 mode, while the inset presents the far-field electric distribution of the A_1 mode. (d) Bloch bands corresponding to the antibonding and bonding magnetic dipole modes, located above and below the light line, respectively. (e) and (f) Field distributions similar to (b) and (c), but for the bonding mode B_1 , which is significantly stronger than the antibonding mode A_1 . The inset emphasizes the predominant light leakage in the in-plane directions.

for the B_1 mode in Figs. 6(e) and 6(f). The in-plane electric field (E_z) distributions reveal that the A_1 mode exhibits antibonding characteristics, while the B_1 mode is bonding. Specifically, the bonding mode features electric hotspots in the gaps between neighboring spheres, whereas the antibonding mode is characterized by null-field distributions.

The far-field distributions shown in the insets further indicate that the bonding mode primarily emits light in the in-plane direction, while the antibonding mode emits comparably strong radiation both in-plane and out-of-plane. Notably, similar to the hole arrays presented in the main text, the out-of-plane scattering pattern of the antibonding mode forms a vortex beam, which results from their common origin in collective MD resonances. The dominance of in-plane emission makes the bonding mode particularly valuable for on-chip applications, where minimizing radiation loss in the out-of-plane direction is crucial.

Figure 7 shows the Bloch bands above the light line

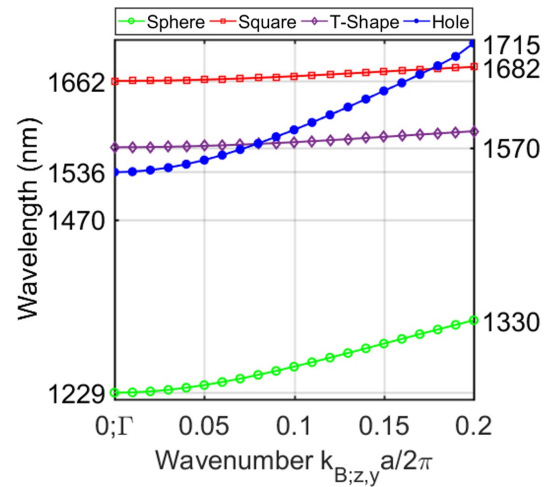


FIG. 7. Bloch bands of the four lattices near the Γ point. The band-edge wavelengths of all four lattices align well with their corresponding collective resonances, highlighting their shared origin in coupled Mie modes.

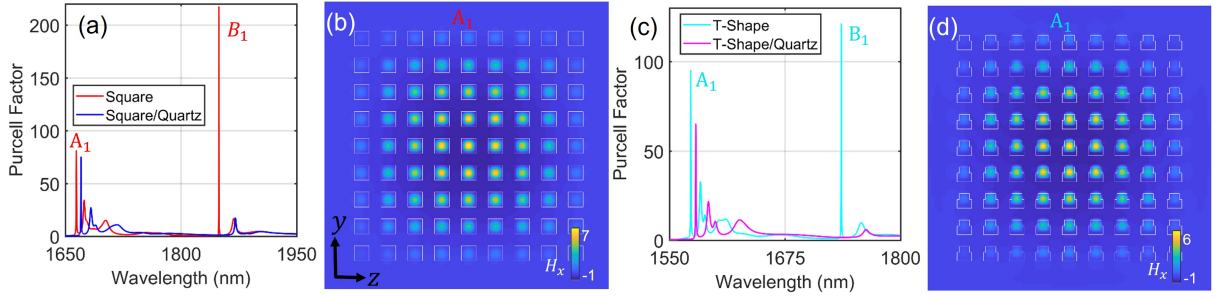


FIG. 8. Effects of symmetry breaking on the interaction between a magnetic dipole m_x at the center of the array. (a) Spectral profile of the Purcell factor for a magnetic dipole interacting with a 9×9 array of square unit cells. Introducing a quartz substrate (refractive index ≈ 1.45) destroys the collective bonding mode B_1 , while the antibonding mode A_1 remains nearly unchanged. (b) Magnetic field (H_x) distribution at the A_1 peak in (a), revealing its origin from collective magnetic dipoles. This collective mode (A_1) generates the vortex beam shown in Fig. 1 of the main text. (c) Breaking the in-plane symmetry by transforming the square unit cells into T-shaped unit cells results in a blue shift of the spectral distribution. Despite this shift, the antibonding (A_1) and bonding (B_1) modes retain comparable resonance strengths. (d) Magnetic near-field distribution of the antibonding (A_1) mode for the T-shaped array, corresponding to the symmetry breaking of the far-field distribution shown in Fig. 1 of the main text.

for the four unit cell geometries discussed in the main text. For comparison, the band structure of the sphere unit cell is replotted from Fig. 6. Variations in geometry lead to shifts in the band-edge wavelengths and changes in dispersion, with the square and T-shaped unit cells exhibiting narrower spectral widths. These results highlight opportunities for dispersion engineering through geometric tuning.

III. IMPACT OF SYMMETRY BREAKING ON COLLECTIVE RESONANCES

This section investigates how in-plane and out-of-plane symmetry breaking influence collective resonances in Miетronic systems. In-plane symmetry breaking is introduced by transforming square unit cells into T-shaped unit cells, while out-of-plane symmetry breaking is induced by incorporating a quartz substrate. These modifications alter the coupling of Mie resonances, resulting in distinct changes in the spectral and spatial properties of the collective modes.

Figure 8(a) presents the spectral profiles of the Purcell factor for a magnetic m_x dipole positioned at the center of a 9×9 square unit cell lattice. Similar to the sphere lattice, the freestanding square lattice supports two well-separated resonant bands, corresponding to the band-edge antibonding and bonding modes labeled A_1 and B_1 , respectively. The A_1 mode corresponds to the band-edge mode with a wavelength of 1662 nm in Fig. 7.

Introducing a quartz substrate disrupts the bonding mode B_1 because this mode extends further into the surrounding environment compared to the antibonding mode, resulting in significant overlap with the extended waves supported by the quartz substrate. Consequently, the substrate strongly suppresses the B_1 resonance. The magnetic H_x field distribution shown in Fig. 8(b) reveals

that the A_1 mode arises predominantly from magnetic dipoles oscillating collectively in the out-of-plane direction, with the collective mode localized near the array's center.

Figures 8(c) and 8(d) show the characteristics of the T-shaped array, which closely resemble those of its square counterpart. Transforming the square shape into a T-shape does not significantly alter the system's underlying geometrical parameters. Consequently, the spectral profiles of the Purcell factor exhibit a blue shift due to the smaller size of the T-shaped unit cells. Both the antibonding A_1 and bonding B_1 modes remain present in the freestanding T-shaped array, as shown in Fig. 8(c). The magnetic near-field [Fig. 8(d)] and electric far-field [Fig. 1(f)] distributions reveal the asymmetry introduced by the T-shaped array.

As with the square array, introducing a quartz substrate destroys the bonding mode B_1 in the T-shaped array (Fig. 8(c)). This occurs because the bonding mode exhibits stronger long-range coupling than its antibonding counterpart. These extended couplings cause the bonding mode to spread out and interact more significantly with its surroundings, making it more susceptible to environmental disturbances that enable energy leakage through the quartz substrate.

IV. FABRY-PÉROT FEEDBACK: MIETRONIC HOLE ARRAYS VS. CONVENTIONAL MIRRORS

In this section, we investigate how hole arrays function as photonic crystal mirrors and compare them to Fabry-Pérot (FP) mirrors formed by four reflective edges. While both types of mirrors confine light within their central region and support FP modes, their underlying mechanisms differ due to the collective nature of the hole arrays.

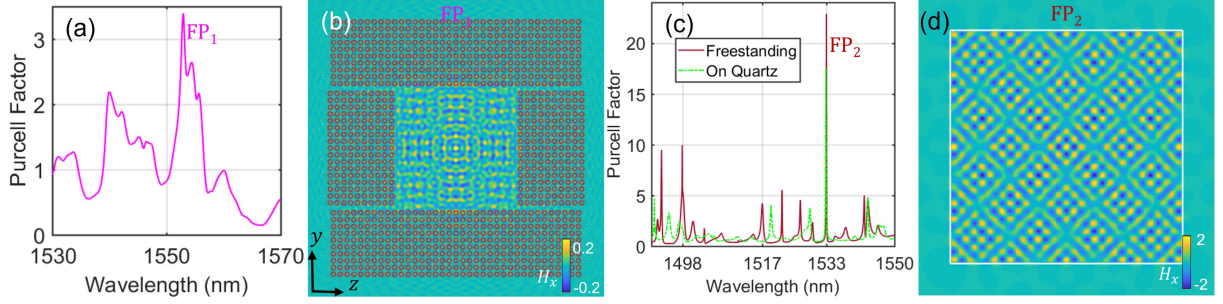


FIG. 9. Light confinement by photonic-crystal mirrors and reflective edges. (a) Spectral profile of the m_x magnetic dipole located at the center of the Fabry-Pérot cavity, formed by removing the 17×17 hole array from the center of the cavity structure shown in Fig. 2 of the main text, with $G_{MC} = 551$ nm. (b) Magnetic H_x field distribution corresponding to the highest peak of the Purcell factor shown in (a). (c) Spectral profiles for both the freestanding cavity and the case with a quartz substrate, with edge sizes corresponding to $G_{MC} = 310$ nm in Fig. 3 of the main text. (d) Magnetic H_x field distribution for the pronounced Fabry-Pérot mode marked in (c).

Conventional edge mirrors backscatter light uniformly across all wavelengths, facilitating the formation of standing wave patterns characteristic of FP modes [44]. In contrast, hole array mirrors exhibit wavelength-dependent backscattering, governed by their interaction with collective Mie modes. This interaction results in distinct optical properties, including enhanced mode selectivity and modified spectral responses.

Figures 9(a) and 9(b) illustrate the interaction between a MD emitter (m_x) and an FP cavity formed by four hole arrays. The bandwidth of the hole-based photonic crystal extends from 1536 nm to beyond 1715 nm, encompassing the peak of the Purcell factor shown in Fig. 9(a). This observation presents a limit of explanations based solely on the photonic crystal framework. Within this framework, the FP cavity can be regarded as a defect, similar to the well-known L_3 photonic crystal cavity [33]. However, in this case, light confinement does not rely on photonic band gaps since the prominent peak in Fig. 9(a) lies within the band-pass region. In contrast, Mie-tronics provides a much clearer picture for understanding the underlying mechanism.

In Mie-tronics, hole arrays collectively act as backscatterers, determining which wavelengths are efficiently reflected based on the number of holes rather than photonic band gaps. These hole arrays also allow partial transmission and radiation leakage into the surrounding free space. As a result, the FP cavity mode observed in Fig. 9(a) remains relatively weak, consistent with the modest field confinement shown in Fig. 9(b). Nonetheless, the field distribution retains the defining features of a typical FP mode, with comparable peak intensities near both the center and the edges of the cavity.

Figures 9(c) and 9(d) show the interaction between an FP cavity formed by four reflective edges and a magnetic dipole m_x placed at its center. The spectral responses in Fig. 9(c) exhibit characteristics typical of FP modes, including evenly spaced resonances and high Q factors. The relatively low peak Purcell factor results from the standing wave being uniformly distributed throughout

the FP cavity, as shown in Fig. 9(d). Despite the high Q factor of the FP mode ($> 10^4$), the relatively small mode volume limits the achievable Purcell enhancement.

Notably, the main text shows that introducing a 17×17 hole array at the center of the FP cavity and fine-tuning the structure significantly increases both the Purcell factor and the Q factor for the hole-based cavity (Fig. 2) compared to the edge-based cavity (Fig. 3), highlighting the collective nature of the hole array.

V. HYBRIDIZATION OF FABRY-PÉROT AND COLLECTIVE MIE RESONANCES

In this section, we investigate the interplay between FP feedback and collective resonances, showing how their hybridization influences optical confinement and resonance properties. By tuning the gap between the four reflective edges and the hole array, we demonstrate how an FP mode and a collective mode can merge, enhancing both the Purcell factor and the Q factor. This analysis highlights the role of Mietronic hole arrays in shaping hybrid resonances, providing insights into optimizing mode confinement and spectral selectivity.

A natural question that follows from the analysis in Section IV is: what happens if we replace the four hole mirrors in Fig. 2 with reflective edges, as shown in Fig. 10(a)? In principle, the edges can act as Fabry-Pérot mirrors, backscattering in-plane leakage and potentially enabling light confinement through the hybridization of multiple trapping mechanisms.

Figure 10(b) shows that such edges can indeed enhance the Q factor, though less effectively than hole mirrors. Instead of the two orders of magnitude increase enabled by collective backscattering from the hole mirrors, we observe only a severalfold improvement—from $Q = 1164$ for the 17×17 hole array in the infinite slab to approximately 6000 for the optimal configuration with $G_{MC} = 120$ nm. This contrast underscores the importance of collective Mie responses in the feedback provided by the hole mir-

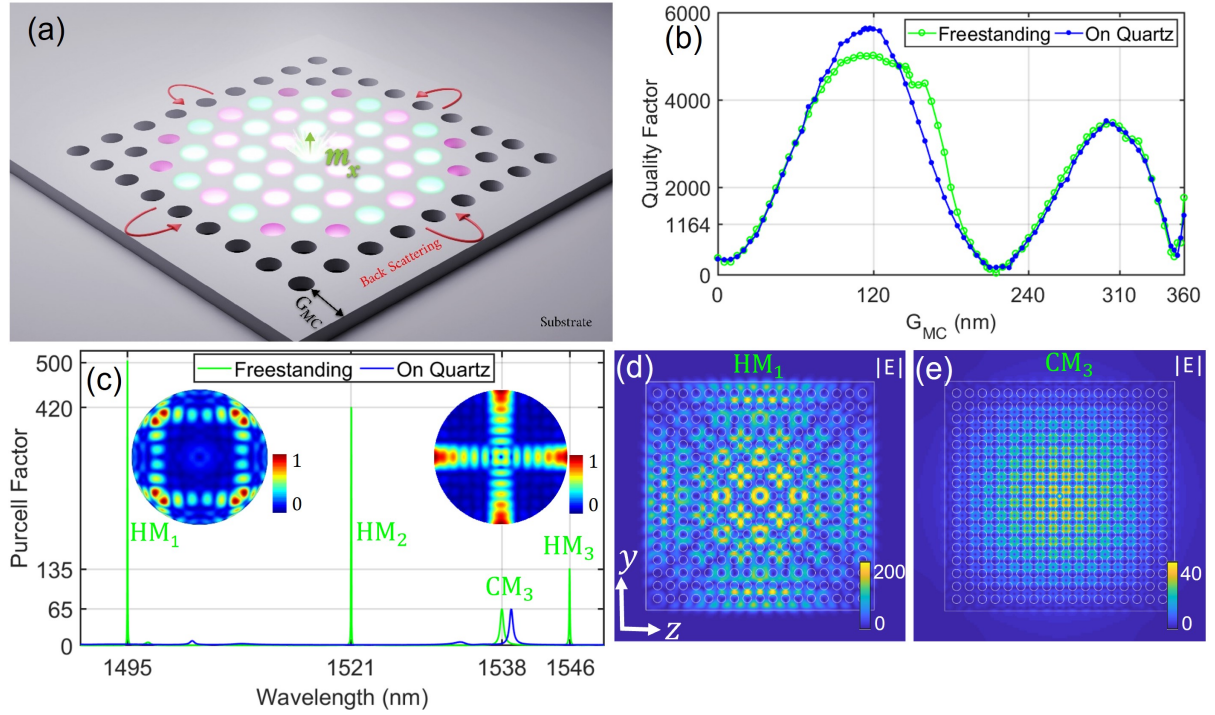


FIG. 10. Unconventional light localization by hybrid modes. (a) Schematic of a magnetic m_x dipole interacting with the hole array on a substrate. The four edges backscatter the in-plane leakage light. (b) Fine-tuning the gap distance between the edges and the 17×17 hole array leads to a significant Q -factor enhancement. Introducing a quartz substrate further boosts the Q factor. (c) Spectral profiles of the Purcell factor for $G_{MC} = 310$ nm exhibits three pronounced hybrid modes, labeled $HM_{1,2,3}$, for the freestanding metastructure. Introducing the substrate destroys all three hybrid modes, while the collective mode (CM_3) remains unaffected. Insets show the far-field distributions of HM_1 and CM_3 . (d) The electric field distribution of HM_1 reveals an unconventional pattern of light localization. (e) Introducing the Fabry-Pérot feedback mechanism enhances light localization in the hole array through collective resonance, compared to that shown in Fig. 2(c) of the main text.

rors: the backscattered waves resonate more efficiently with the central trapped mode when the feedback is collective rather than geometric.

In realistic systems, mechanical stability is often ensured using a quartz substrate. Interestingly, the presence of such a substrate further enhances the Q factor near the optimal edge configuration, as seen in Fig. 10(b). This suggests that vertical symmetry breaking can also improve the localization.

More strikingly, Fig. 10(c) reveals hybrid modes— HM_1 , HM_2 , and HM_3 —with Purcell factors and Q values that surpass those of the collective mode CM_3 . These hybrid modes exhibit uniformly spaced spectral peaks, reminiscent of Fabry-Pérot resonances, but their spatial and angular profiles reveal a more complex origin. As shown in the insets of Fig. 10(c), the characteristic vortex beams remain visible, but are no longer dominant. Instead, radiation into multiple channels takes over, signaling the interplay of distinct wave localization mechanisms.

To further understand unconventional light localization through multiple feedback mechanisms, we present the near-field distributions corresponding to the HM_1 and CM_3 modes in Figs. 10(d) and 10(e). The localized pattern of the HM_1 peak cannot be explained by a single

feedback mechanism, such as a Fabry-Pérot cavity, a low-order whispering gallery cavity, or a collective Mie resonance alone. Although Fig. 10(e) shows that the CM_3 peak is dominated by the collective resonance of magnetic dipoles, its far-field pattern in Fig. 10(c)—dominated by radiation into large-angle directions—indicates that contributions from the Fabry-Pérot feedback mechanism cannot be neglected.

Figure 11 illustrates how the merging of hybrid and collective modes underlies the Q enhancement observed in Fig. 10(b). At $G_{MC} = 0$ nm, two hybrid modes, HM_4 and HM_5 , emerge within the spectral range. Compared to the distribution shown in Fig. 9(c), the introduction of the hole array leads to a sparser set of hybrid modes accompanied by significantly enhanced Purcell factors—features that are particularly advantageous for applications such as single-mode nanolasers.

As G_{MC} increases, the hybrid modes redshift linearly due to their FP nature, whereas the collective mode remains spectrally stable around 1539 nm. At $G_{MC} = 120$ nm, the collective mode reaches its optimal value, significantly enhanced compared to the red peak at $G_{MC} = 0$ nm. At this point, the hybrid mode merges into the collective mode, acting as an auxiliary resonance that boosts the latter's response. Introducing the quartz sub-

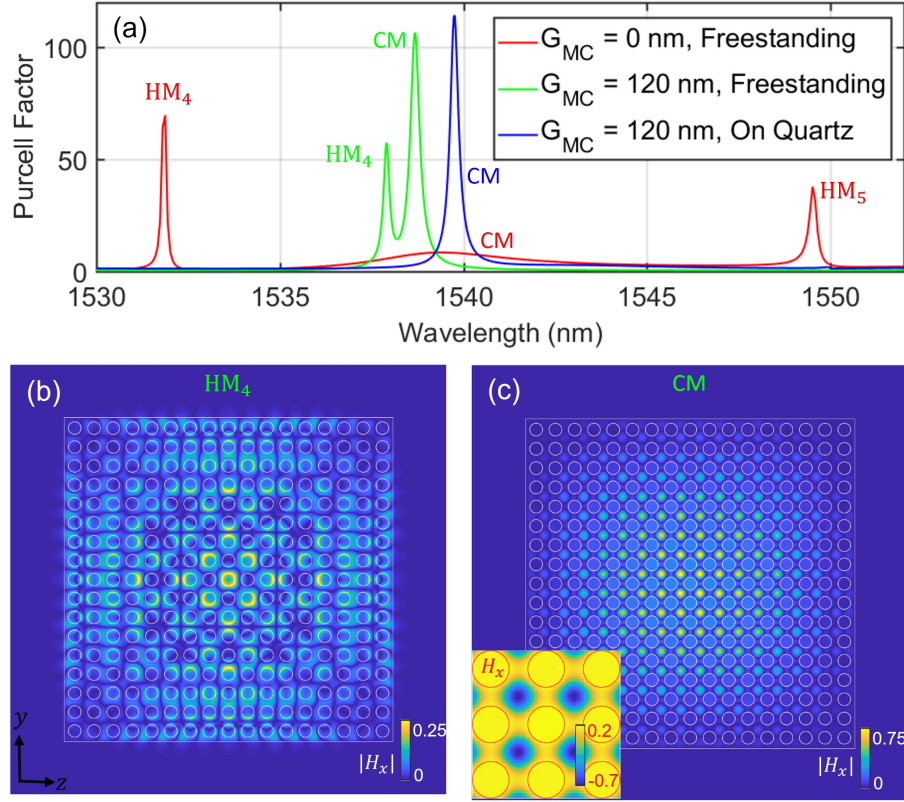


FIG. 11. Merging of hybrid and collective modes and the effects of the quartz substrate. (a) Spectral profiles of the Purcell factor associated with a magnetic m_x dipole placed at the cavity center. (b) and (c) Magnetic H_x field distributions for the collective mode (CM) and the hybrid mode (HM_4), respectively. The inset in (c) shows the imaginary component of H_x , revealing the opposite magnetic field directions in the hole-centered and the silicon-centered unit cells.

strate suppresses the hybrid modes but leaves the collective mode intact, consistent with observations in both square and T-shaped arrays. This robustness highlights their shared origin in antibonding collective MD resonances.

Figures 11(b) and 11(c) show the magnetic near-field distributions of the hybrid mode HM_4 and the collective mode. A detailed examination of Fig. 11(c) reveals that a significant portion of the magnetic field is concentrated inside the holes. This is further illustrated in the inset, which shows the imaginary component of the magnetic field. The positive and negative values correspond to field directions along the positive and negative x -axis, respectively. These magnetic field components inside the holes are indicative of Mie void modes [54]. The presence of such void modes distinguishes the hole structure from sphere, square, and T-shaped lattices, enabling the unconventional localization observed in the hybrid modes. The distinct near-field patterns of HM_4 , shown in Fig. 11(b), further highlights the unique electromagnetic behavior of the hole structure, especially in contrast to conventional reflective-edge geometries.

These results illustrate a broader principle: light can be localized through the constructive interference of multiple feedback mechanisms. The Fabry-Pérot reflections,

substrate-induced confinement, and collective resonances do not act in isolation, but reinforce each other in ways that enable high- Q , hybridized modes beyond what any single mechanism can achieve.

VI. ORIGIN OF FLATBANDS IN TWISTED MOIRÉ METASTRUCTURE

This section further investigates interband coupling in twisted moiré metastructures and its impact on light localization and flatband formation.

Figure 12(a) shows the full spectral range of band HX_1 in the hexagonal hole metastructure discussed in the main text. In the untwisted structure ($\theta = 0^\circ$), this band is spectrally broad and dominated by the collective band-edge mode HX_1 . Introducing a twist ($\theta = 1.45^\circ$) induces macroscopic degeneracy, compressing this broad band into a few distinct, extremely narrow spectral peaks. While HX_1 and its twisted counterpart tHX_1 are discussed in the main text, the inset in Fig. 12(a) reveals two additional modes, labeled M_1 and M_2 . Interestingly, the magnetic field distributions of M_1 and M_2 in Figs. 12(b) and 12(c) indicate that they originate from band HX_2 . This suggests that, unlike in the untwisted metas-

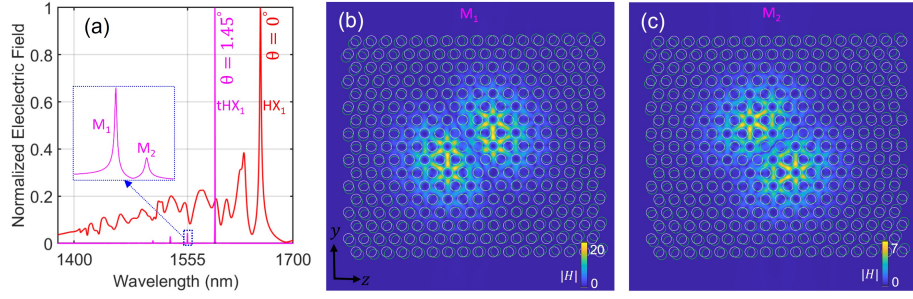


FIG. 12. Weaker collective resonances in the twisted metastructure. (a) Normalized electric field spectra of the excited modes in the hexagonal hole array ($\theta = 0^\circ$) and its twisted counterpart ($\theta = 1.45^\circ$), with the dipole source μ_x at the center. The inset highlights two resonant modes around 1555 nm, labeled M_1 and M_2 , which are weaker than tHX_1 . (b) and (c) Magnetic field distributions of M_1 and M_2 , showing their common origin from band HX_1 . In contrast, the main text discusses HX_1 and its twisted version tHX_1 , which originate from band HX_1 . This indicates that in the twisted metastructure, both bands strongly interact with the dipole source.

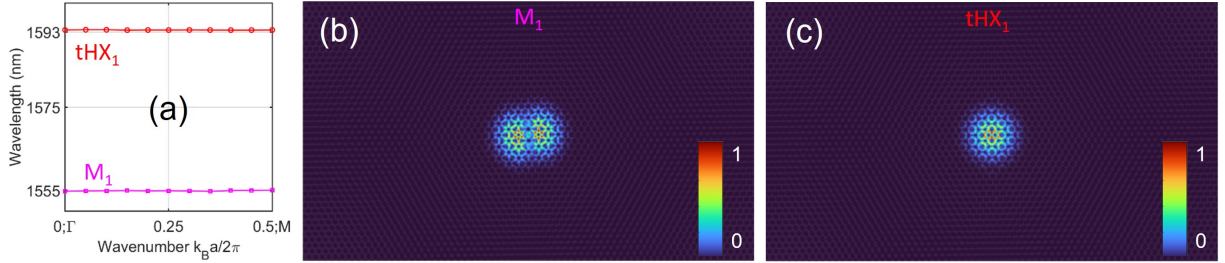


FIG. 13. Origin of moiré flatbands. (a) Two flatbands obtained by applying Bloch boundary conditions to the moiré unit cell corresponding to a twist angle of $\theta = 1.45^\circ$. (b) and (c) Magnetic field distributions of the eigenmodes associated with the flatbands in (a) reveal their tightly confined nature. This strong spatial confinement, together with the positive energy of light, renders the moiré modes insensitive to the imposed Bloch boundary conditions, giving rise to superflatbands.

structure, the dipole source in the twisted metastructure strongly couples to both bands. Furthermore, the mode profiles of M_1 and M_2 clearly highlight their second-order collective nature, characterized by a null magnetic field at the cavity center [44].

Although moiré structures form true crystals only at specific discrete twist angles, both theoretical and experimental studies have shown that quasi-crystal moiré structures exhibit similar phenomena to their crystalline counterparts [55]. Figure 13 explains this observation from the perspective of Mie-tronics. The two collective modes are strongly localized at the cavity center, and most of the light leaks out in the out-of-plane direction. This effectively decouples the localized modes in neighboring moiré supercells, rendering the eigenmodes insensitive to Bloch boundary conditions. Both the flatband wavelengths in Fig. 13(a) and the field distributions in Figs. 13(b)-(c) indicate that these flatbands originate from the twisted collective resonances shown in Fig. 12(a).

VII. IMPACT OF GEOMETRIC DISORDER ON LIGHT LOCALIZATION IN MOIRÉ CAVITY

To understand how geometric disorder—such as that introduced during fabrication—affects light localization in moiré cavities, we impose controlled variations in hole diameter (σ_D) and position (σ_{yz}). Specifically, $\sigma_D = 30$ nm corresponds to pseudorandom diameters D_h drawn from the interval [335, 365] nm. Similar definitions apply to positional disorder in the y and z directions [12]. For each case, we simulate 15 disordered samples and evaluate their Q factors, as summarized in Fig. 14.

The results show that disorder significantly weakens the collective band-edge resonance, as evidenced by large reductions in Q . In Fig. 14(b), certain collective modes vanish from the Purcell factor spectra but remain detectable in the spectral profiles of the magnetic field recorded at the cavity center. Their corresponding Q values are extracted from the field decay curves.

As the disorder increases from Fig. 14(a) to Fig. 14(c), the constituent resonances become progressively weaker, undermining the twisted mode that arises from their interference. The associated spectral peaks also become more distinct, reducing spectral overlap and thereby weakening coherent backscattering. This leads to en-

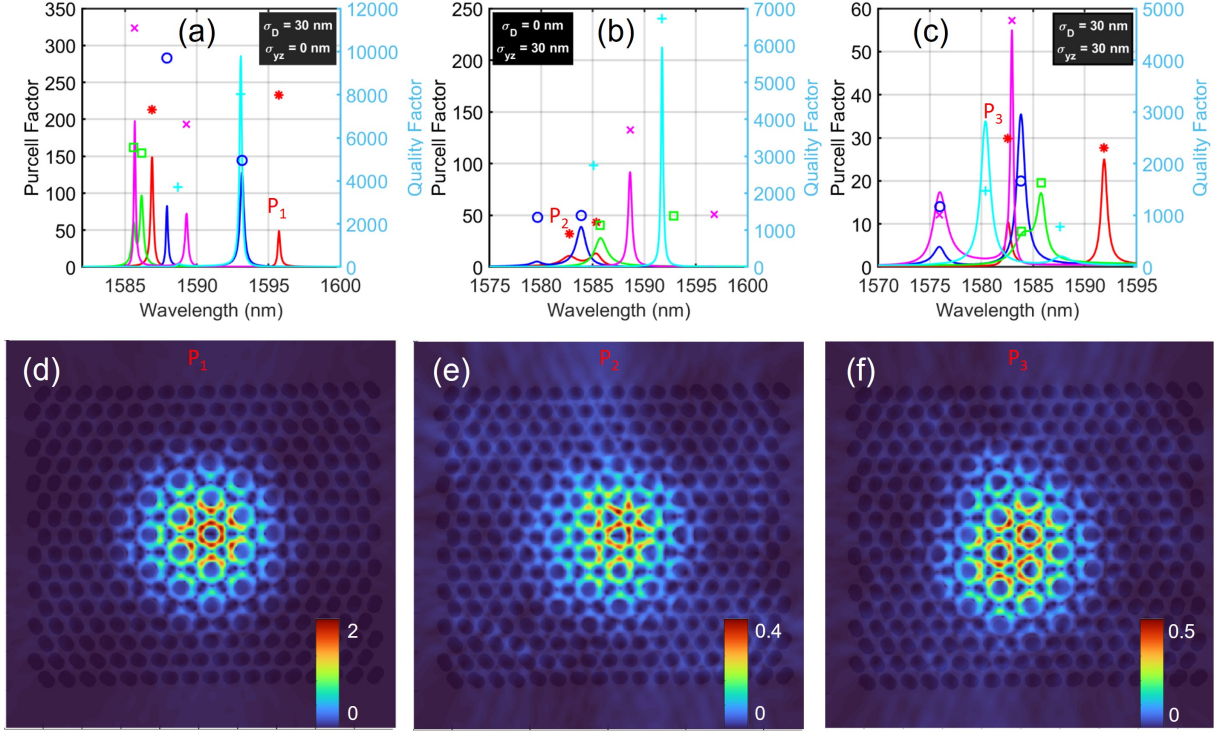


FIG. 14. Effects of diameter and positional disorders of holes on the resonance at the magic angle $\theta = 1.5^\circ$. (a) A diameter disorder of $\sigma_D = 30$ nm reduces both the Purcell and Q factors by more than an order of magnitude and spectrally splits the two collective resonances. (b) A positional disorder of $\sigma_{yz} = 30$ nm leads to an even greater reduction in both metrics compared to (a). (c) When both diameter and positional disorders are introduced simultaneously, the Purcell and Q factors drop further, compounding the effects observed in (a) and (b). (d)–(f) Magnetic field distributions of the three disordered modes marked in (a)–(c) show that disorder weakens light localization by enhancing in-plane leakage.

hanced radiation losses in both in-plane and out-of-plane directions. The increased in-plane leakage is evident in Figs. 14(d)–(f), which show the magnetic field distributions of the disordered collective resonances marked in Figs. 14(a)–(c). Importantly, the larger spectral splitting induced by disorder does not indicate stronger cou-

pling between the resonant modes. This counterintuitive behavior underscores the subtle and complex interplay among interference, localization, and radiation in Metronic systems.

-
- [1] N. A. Logan, Survey of some early studies of the scattering of plane waves by a sphere, *Proceedings of the IEEE* **53**, 773 (1965).
 - [2] Y. Kivshar, The rise of Mie-tronics, *Nano Letters* **22**, 3513 (2022).
 - [3] S. John, Localization of light, *Physics Today* **44**, 32 (1991).
 - [4] K. J. Vahala, Optical microcavities, *Nature* **424**, 839 (2003).
 - [5] P. W. Anderson, Absence of diffusion in certain random lattices, *Physical Review* **109**, 1492 (1958).
 - [6] S. John, Strong localization of photons in certain disordered dielectric superlattices, *Physical Review Letters* **58**, 2486 (1987).
 - [7] A. Lagendijk and B. A. Van Tiggelen, Resonant multiple scattering of light, *Physics Reports* **270**, 143 (1996).
 - [8] D. S. Wiersma, P. Bartolini, A. Lagendijk, and R. Righini, Localization of light in a disordered medium, *Nature* **390**, 671 (1997).
 - [9] P. Hsieh, C. Chung, J. McMillan, M. Tsai, M. Lu, N. Panou, and C. W. Wong, Photon transport enhanced by transverse anderson localization in disordered superlattices, *Nature Physics* **11**, 268 (2015).
 - [10] A. Yamilov, S. E. Skipetrov, T. W. Hughes, M. Minkov, Z. Yu, and H. Cao, Anderson localization of electromagnetic waves in three dimensions, *Nature Physics* **19**, 1308 (2023).
 - [11] T. X. Hoang, D. Leykam, and Y. Kivshar, Photonic flat-band resonances in multiple light scattering, *Physical Review Letters* **132**, 043803 (2024).
 - [12] T. X. Hoang, D. Leykam, H.-S. Chu, C. E. Png, F. J. Garcia-Vidal, and Y. S. Kivshar, Collective nature of high-Q resonances in finite-size photonic metastructures, *Physical Review Research* **7**, 013316 (2025).

- [13] G. Tarnopolsky, A. J. Kruchkov, and A. Vishwanath, Origin of magic angles in twisted bilayer graphene, *Physical Review Letters* **122**, 106405 (2019).
- [14] H. Wang, S. Ma, S. Zhang, and D. Lei, Intrinsic superflat bands in general twisted bilayer systems, *Light: Science & Applications* **11**, 159 (2022).
- [15] G. Yu, Y. Wang, M. I. Katsnelson, and S. Yuan, Origin of the magic angle in twisted bilayer graphene from hybridization of valence and conduction bands, *Physical Review B* **108**, 045138 (2023).
- [16] G. Mie, Contributions to the optics of turbid media, particularly of colloidal metal solutions, *Annalen der Physik* **25**, 377 (1976).
- [17] T. Wriedt, Mie theory: a review, *The Mie theory: Basics and applications*, 53 (2012).
- [18] A. D. Utyushev, V. I. Zakomirnyi, and I. L. Rasskazov, Collective lattice resonances: Plasmonics and beyond, *Reviews in Physics* **6**, 100051 (2021).
- [19] P. W. Anderson, The question of classical localization: A theory of white paint?, *Philosophical Magazine B* **52**, 505 (1985).
- [20] See Supplemental Material.
- [21] A. Devaney and E. Wolf, Multipole expansions and plane wave representations of the electromagnetic field, *Journal of Mathematical Physics* **15**, 234 (1974).
- [22] T. X. Hoang, X. Chen, and C. J. Sheppard, Multipole and plane wave expansions of diverging and converging fields, *Optics Express* **22**, 8949 (2014).
- [23] R. Richtmyer, Dielectric resonators, *Journal of Applied Physics* **10**, 391 (1939).
- [24] W. C. Chew and Y. Wang, Efficient ways to compute the vector addition theorem, *Journal of Electromagnetic Waves and Applications* **7**, 651 (1993).
- [25] T. X. Hoang, S. N. Nagelberg, M. Kolle, and G. Barbastathis, Fano resonances from coupled whispering-gallery modes in photonic molecules, *Optics Express* **25**, 13125 (2017).
- [26] M. S. Rider, A. Buendia, D. R. Abujetas, P. A. Huidobro, J. A. Sanchez-Gil, and V. Giannini, Advances and prospects in topological nanoparticle photonics, *ACS photonics* **9**, 1483 (2022).
- [27] A. Yariv, Y. Xu, R. K. Lee, and A. Scherer, Coupled-resonator optical waveguide: a proposal and analysis, *Optics Letters* **24**, 711 (1999).
- [28] S. I. Azzam and A. V. Kildishev, Photonic bound states in the continuum: from basics to applications, *Advanced Optical Materials* **9**, 2001469 (2021).
- [29] Y. Chen, M. Wang, J. Si, Z. Zhang, X. Yin, J. Chen, N. Lv, C. Tang, W. Zheng, Y. Kivshar, *et al.*, Observation of chiral emission enabled by collective guided resonances, *Nature Nanotechnology*, 1 (2025).
- [30] Z. Chen, X. Yin, J. Jin, Z. Zheng, Z. Zhang, F. Wang, L. He, B. Zhen, and C. Peng, Observation of miniaturized bound states in the continuum with ultra-high quality factors, *Science Bulletin* **67**, 359 (2022).
- [31] Z. Liu, Y. Xu, Y. Lin, J. Xiang, T. Feng, Q. Cao, J. Li, S. Lan, and J. Liu, High-Q quasibound states in the continuum for nonlinear metasurfaces, *Physical Review Letters* **123**, 253901 (2019).
- [32] K. Koshelev, S. Lepeshov, M. Liu, A. Bogdanov, and Y. Kivshar, Asymmetric metasurfaces with high- q resonances governed by bound states in the continuum, *Phys. Rev. Lett.* **121**, 193903 (2018).
- [33] T. X. Hoang, H.-S. Chu, F. J. García-Vidal, and C. E. Png, High-performance dielectric nano-cavities for near- and mid-infrared frequency applications, *Journal of Optics* **24**, 094006 (2022).
- [34] A. C. Overvig, S. C. Malek, M. J. Carter, S. Shrestha, and N. Yu, Selection rules for quasibound states in the continuum, *Physical Review B* **102**, 035434 (2020).
- [35] G. Li, A. Luican, J. Lopes dos Santos, A. Castro Neto, A. Reina, J. Kong, and E. Andrei, Observation of Van Hove singularities in twisted graphene layers, *Nature Physics* **6**, 109 (2010).
- [36] R. Bistritzer and A. H. MacDonald, Moiré bands in twisted double-layer graphene, *Proceedings of the National Academy of Sciences* **108**, 12233 (2011).
- [37] X.-R. Mao, Z.-K. Shao, H.-Y. Luan, S.-L. Wang, and R.-M. Ma, Magic-angle lasers in nanostructured moiré superlattice, *Nature Nanotechnology* **16**, 1099 (2021).
- [38] A. Raun, H. Tang, X. Ni, E. Mazur, and E. L. Hu, GaN magic angle laser in a merged moiré photonic crystal, *ACS Photonics* **10**, 3001 (2023).
- [39] I. Awai and Y. Zhang, Coupling coefficient of resonators—an intuitive way of its understanding, *Electronics and Communications in Japan (Part II: Electronics)* **90**, 11 (2007).
- [40] H.-Y. Luan, Y.-H. Ouyang, Z.-W. Zhao, W.-Z. Mao, and R.-M. Ma, Reconfigurable moiré nanolaser arrays with phase synchronization, *Nature* **624**, 282 (2023).
- [41] T. X. Hoang, X. Chen, and C. J. Sheppard, Rigorous analytical modeling of high-aperture focusing through a spherical interface, *JOSA A* **30**, 1426 (2013).
- [42] T. X. Hoang, X. Chen, and C. J. Sheppard, Interpretation of the scattering mechanism for particles in a focused beam, *Physical Review A—Atomic, Molecular, and Optical Physics* **86**, 033817 (2012).
- [43] L. Rayleigh, The problem of the whispering gallery, *Scientific papers* **5**, 617 (1912).
- [44] T. X. Hoang, S. T. Ha, Z. Pan, W. K. Phua, R. Paniagua-Domínguez, C. E. Png, H.-S. Chu, and A. I. Kuznetsov, Collective Mie resonances for directional on-chip nanolasers, *Nano Letters* **20**, 5655 (2020).
- [45] G. H. Wannier, The structure of electronic excitation levels in insulating crystals, *Physical Review* **52**, 191 (1937).
- [46] G. H. Wannier, Dynamics of band electrons in electric and magnetic fields, *Reviews of Modern Physics* **34**, 645 (1962).
- [47] A. Marrazzo, S. Beck, E. R. Margine, N. Marzari, A. A. Mostofi, J. Qiao, I. Souza, S. S. Tsirkin, J. R. Yates, and G. Pizzi, Wannier-function software ecosystem for materials simulations, *Reviews of Modern Physics* **96**, 045008 (2024).
- [48] F. Scheffold, R. Lenke, R. Tweert, and G. Maret, Localization or classical diffusion of light?, *Nature* **398**, 206 (1999).
- [49] D. S. Wiersma, J. G. Rivas, P. Bartolini, A. Lagendijk, and R. Righini, Localization or classical diffusion of light?, *Nature* **398**, 207 (1999).
- [50] A. Yamilov, H. Cao, and S. E. Skipetrov, Anderson transition for light in a three-dimensional random medium, *Physical Review Letters* **134**, 046302 (2025).
- [51] L. Sapienza, H. Thyrrstrup, S. Stobbe, P. D. Garcia, S. Smolka, and P. Lodahl, Cavity quantum electrodynamics with anderson-localized modes, *Science* **327**, 1352 (2010).
- [52] A. Lagendijk, B. v. Tiggelen, and D. S. Wiersma, Fifty years of Anderson localization, *Physics Today* **62**, 24

- (2009).
- [53] L. Rayleigh, XVIII. On the passage of electric waves through tubes, or the vibrations of dielectric cylinders, The London, Edinburgh, and Dublin Philosophical Magazine and Journal of Science **43**, 125 (1897).
 - [54] M. Hentschel, K. Koshelev, F. Sterl, S. Both, J. Karst, L. Shamsafar, T. Weiss, Y. Kivshar, and H. Giessen, Dielectric Mie voids: confining light in air, Light: Science & Applications **12**, 3 (2023).
 - [55] H. Wang, S. Ma, S. Zhang, and D. Lei, Intrinsic superflat bands in general twisted bilayer systems, Light: Science & Applications **11**, 159 (2022).